Applied Catalysis B: Environmental 286 (2021) 119853

Contents lists available at ScienceDirect

Applied Catalysis B: Environmental

journal homepage: www.elsevier.com/locate/apcatb

Z-scheme transition metal bridge of Co_9S_8/Cd/CdS tubular heterostructure for enhanced photocatalytic hydrogen evolution

Tianxi Zhang [a,1], Fanlu Meng [b,1], Yin Cheng [b], Nikita Dewangan [a], Ghim Wei Ho [b,c,**], Sibudjing Kawi [a,*]

[a] Department of Chemical & Biomolecular Engineering, National University of Singapore, 4 Engineering Drive 4, 117585, Singapore
[b] Department of Electrical and Computer Engineering, National University of Singapore, 4 Engineering Drive 3, 117583, Singapore
[c] Institute of Materials Research and Engineering, A*STAR (Agency for Science, Technology and Research), 3 Research Link, 117602, Singapore

ARTICLE INFO

Keywords:
Cadmium sulfide
Cobalt sulfide
Photocatalytic H_2evolution
Light absorption
Charge transfer

ABSTRACT

Narrow band gap semiconductors heterojunction with superior coupling and composition matching can enhance light absorption, reduce carrier recombination and increase redox activity. Here, we report Co_9S_8/Cd/CdS Z-scheme type heterojunctions with hierarchical tubular heterostructure and inexpensive transition metallic electronic bridge between two distinct semiconductors by a simultaneous immobilization and *in-situ* reduction strategy. The designed heterostructure greatly promotes the redox activity owing to high-density catalytic sites, excellent visible light capture by small band gap Co_9S_8/CdS and hollow framework in conjunction with fast charge separation and smooth transfer through intermediary conductive Cd. The optimized photocatalyst exhibits a hydrogen generation rate up to 10.42 μmol h^{-1} without obvious drop in performance over multiple cycles. The structural design, matching tandem constituent and continuous phase mediator are the pivotal factors to engender an efficient solid-state Z-scheme photocatalysis. The facile synthetic approach and noble metal free tandem structure of this work provide alternative avenues for the development of heterojunction photocatalysts for efficient solar-to-chemical conversion.

1. Introduction

Solar-fuel conversion ranks the highest potential to revolutionize energy supply to achieve the goal of low carbon economy and sustainable development [1–5]. Particularly, photocatalytic water splitting powered by renewable solar is one of the most attractive measures to produce green hydrogen energy, widely recognized as an ideal clean, storable and versatile alternative fuel [6–8]. Among numerous photocatalyst candidates [9–12], metal chalcogenides possess many advantages, such as earth abundance, controllable morphology, desirable narrow bandgap, accelerated charge transfer and excellent active sites [13–15]. Rational coupling of hybrid metal chalcogenides can satisfy the high requirements of wide solar spectrum absorption and appropriate redox potential for efficient photocatalytic activity [16,17].

CdS is a prominent classical metal chalcogenide widely used in photocatalytic reactions of many kinds, particularly in hydrogen evolution and water splitting [18–22]. Be that as it may, CdS has shortcomings including high electron-hole pair annihilation, photo-corrosion and instability which calls for judicious catalyst design [23–25]. Constructing Z-scheme type heterojunctions by coupling complementary semiconductors has been commonly adopted [26–28]. By virtue of narrow bandgap and high flat-band potential of more negative than the water reduction potential qualifies Co_9S_8 as a favorable counterpart of CdS. Meanwhile, the desirable shared sulfur atom between the two semiconductors further boosts the intermolecular interactions for efficient charge transfer process [29–31]. In addition, the insertion of a metallic shuttle redox mediator at the heterojunctions can assist the separation and migration of charges [32,33]. For instance, in typical three components Z-scheme photocatalysts, noble metal nanoparticles, carbon-based graphene, carbon nanotubes and quantum dots are employed as solid state mediator [34–36]. However, developing Z-scheme nanostructures with enhanced intrinsic conductivity, interfacial contact and high stability is a nontrivial task, due to the seemingly complex multiple steps needed for synthesis and/or modifications

* Corresponding author.
** Corresponding author at: Department of Electrical and Computer Engineering, National University of Singapore, 4 Engineering Drive 3, 117583, Singapore.
E-mail addresses: elehgw@nus.edu.sg (G.W. Ho), chekawis@nus.edu.sg (S. Kawi).
[1] These authors contributed equally.

https://doi.org/10.1016/j.apcatb.2020.119853
Received 2 November 2020; Received in revised form 19 December 2020; Accepted 19 December 2020
Available online 4 January 2021

processes which often not result in improved performance instead result in the destruction of active components and structure [37–40]. On this note, maintaining continuity and compatibility of component constituents between the heterojunctions using facile synthetic route is worthy of consideration.

Herein, we report a rationally designed hybrid transition metal dichalcogenides Z-scheme photocatalyst for hydrogen generation by effective coupling of visible-light responsive Co_9S_8 and complex Cd/CdS nanoparticles. Few crucial factors namely structural design, materials choice and interface are considered in the design of the solid state Z-scheme that is free from unstable ionic redox or expensive noble metal conductor shuttle. Specifically, as shown in Scheme 1 one-dimensional (1D) Co_9S_8 hollow-tube is exploited for its merits of increased surface active sites and short charge diffusion length through the radial tube thickness. Facile *in-situ* reduction of Cd with CdS and direct growth on Co_9S_8 ensure intimate contact and interfacial compatibility between mixed composites thus ensuring a smooth charge migration bridge between the two semiconductors. The direct incorporation of Cd between CdS and Co_9S_8 offers a good electronic mediator interface, on account of its metallic conductivity and localized formation during CdS preparation that resulted in heterojunctions of close contact and high stability. This pivotal design configuration would undoubtedly promote the separation and migration of photo-generated electrons-holes, and enhanced photocatalytic activity. Based on a series of structure and composition exploration, the optimized composite could achieve a remarkably improved hydrogen evolution rate (by 570 %) and cycling stability under visible-light illumination. This work provides a rational design and construction of solid state Z-scheme heterojunction for effective spatial separation of the reductive and oxidative active sites that greatly improved the photocatalytic performance.

2. Experimental section

2.1. Chemicals

Urea (CH_4N_2O), cobalt chloride hexahydrate ($CoCl_2{\cdot}6H_2O$), cadmium chloride anhydrous ($CdCl_2$) and thiourea (CH_4N_2S) were all purchased from Sigma Aldrich. Citric acid trisodium salt dihydrate ($C_6H_5Na_3O_7$ $2H_2O$) was purchased from VWR international Ltd. Sodium sulfide hydrate (Na_2S, 60–63 %) was bought from Acros Organics. All chemicals were used without any purification.

2.2. Preparation of photocatalysts

2.2.1. Preparation of Co_9S_8 nanotubes

Co_9S_8 nanotubes were prepared using sacrificial template method upon Kirkendall effect. $Co(CO_3)_{0.35}Cl_{0.20}(OH)_{1.10}$ nanowires were firstly synthesized as hard templates. In a typical experimental procedure, urea (5 mmol) and cobalt chloride hexahydrate (5 mmol) were dissolved in deionized (DI) water (30 ml) with intense stirring for 10 min. Then, the mixed pink solution was transferred into a 50 ml autoclave and kept at 120 °C for 10 h. After cooling down to room temperature naturally, the precipitates were collected and washed with DI water, ethanol several times and dried at 60 °C for 12 h. The obtained $Co(CO_3)_{0.35}Cl_{0.20}(OH)_{1.10}$ nanowires (110 mg) were dispersed into 40 ml of Na_2S aqueous solution (5 mg/ml) with strong stirring and ultrasonic treatment and were then transferred into a 50 ml autoclave and kept at 160 °C for 8 h. Similar washing and drying process was adopted for the produced black precipitates.

2.2.2. Preparation of hierarchical Co_9S_8/Cd/CdS tubular heterostructures

Cd/CdS nanoparticles were grown directly on Co_9S_8 nanotubes *via* hydrothermal methods. In a typical procedure, a certain amount of Co_9S_8 nanotubes (e.g. 2 mg, 5 mg, 10 mg and 15 mg) was dispersed into 30 ml DI water with ultrasonic for 30 min to form a homogeneous suspension. Afterwards, $CdCl_2$ (0.5 mmol) and a certain amount of citric acid trisodium salt dihydrate were added and stirred for 2 h. 0.5 mmol thiourea was then put into the above solution, which was quickly transferred into 50 ml autoclave and kept at 160 °C for 5 h. When the temperature cooled down to room temperature, the precipitates were collected and dried at 60 °C in vacuum overnight. The obtained samples were labeled as CC-2, CC-5, CC-10 and CC-15, respectively.

For comparison, pure Cd/CdS samples were prepared without Co_9S_8 under same experimental parameters except for reaction time and the amount of citric acid trisodium salt dihydrate. For Cd/CdS-1, 5 h of reaction time and 0.1 g of citric acid trisodium salt dihydrate were used. For Cd/CdS-2, reaction time was only kept for 2 h with the same amount of citric acid trisodium salt dihydrates as Cd/CdS-1. For Cd/CdS-3, reaction time was still 5 h, but citric acid trisodium salt dihydrate was increased to 0.3 g. For control samples, bare CdS without Cd nanoparticles were prepared following Yang's methods with some modification [41].

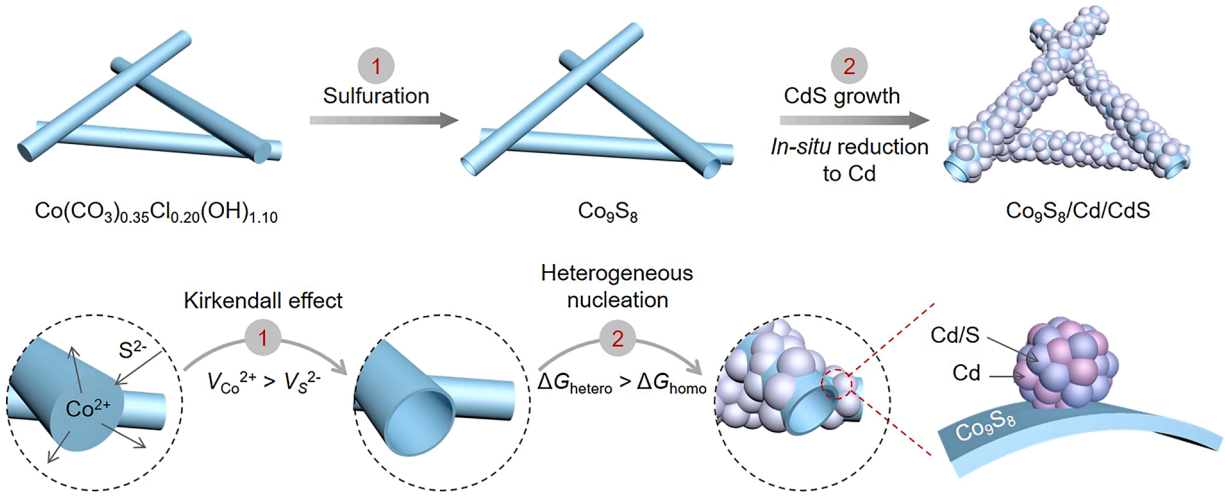

Scheme 1. Schematic diagram illustrating synthesis process of the Co_9S_8@Cd/CdS heterostructure.

2.3. Characterization of photocatalysts

Scanning electron microscopy (SEM) images were taken using a JEOL FEG JSM 7001 F. Transmission electron microscopic (TEM), high resolution transmission electron microscope (HRTEM) images, high angle annular dark field-scanning transmission electron microscopy (HAADF-STEM), and elemental mapping images were collected by a JEOL JEM-2100 F. X-ray diffraction patterns were obtained from a D5005 Bruker X-ray diffractometer equipped with graphite-monochromated Cu Kα radiation at $\lambda = 1.541$ Å). X-ray photoelectron spectroscopy (XPS) was performed on Kratos AXIS Ultra DLD with a monochromatic Al Kα X-ray source (1486.6 eV) for surface analysis. UV–vis absorption spectra were collected on a Shimadzu UV-3600 UV–vis spectrophotometer. The photoluminescence (PL) was detected with 440 nm excitation wavelength by Shimadzu RF-5301 PC series of fluorescence spectrometers.

2.4. Photocatalytic activity test

The H_2 evolution measurements were carried out in a sealed quartz glass vial. A commercial 300 W Xenon lamp with a UV cutoff filter ($\lambda \geq 400$ nm) was used to simulate the visible-light source with a light intensity of 100 mW/cm^2. Specifically, 2 mg photocatalyst was first dispersed into 10 ml aqueous solution containing 0.35 M Na_2S and 0.25 M Na_2SO_3 as sacrificial reagents, and the quartz vial and solution was then purged using Ar flow for 15 min. The produced gas mixtures were analyzed by injecting 100 μL gas samples into gas chromatograph (Shimadzu, GC-2014AT) every hour to calculate the H_2 evolution rate.

2.5. Photoelectrochemical measurements

All photoelectrochemical measurements were performed on a CHI 660E electrochemical workstation with three-electrode configuration. The prepared catalysts were coated onto ITO substrates and used as working electrode, a platinum plate and saturated calomel electrode (SCE) electrode were used as counter and reference electrode, respectively. 0.5 M Na_2SO_4 aqueous solution was used as electrolyte. The photocurrent responses were recorded at open-circuit potential under chopped visible-light irradiation. Electrochemical impedance spectroscopy (EIS) was also performed at open-circuit potential with a frequency loop from 100 kHz to 0.1 Hz by applying a sine wave with an amplitude of 5 mV.

3. Results and discussion

3.1. Morphological characterization of Co_9S_8/Cd/CdS tubular heterostructure

The morphological structure evolution and constituent transformation from $Co(CO_3)_{0.35}Cl_{0.20}(OH)_{1.10}$ nanowires to Co_9S_8 nanotubes were firstly investigated by SEM, TEM and EDX elemental mapping (Fig. 1). Fig. 1a shows that $Co(CO_3)_{0.35}Cl_{0.20}(OH)_{1.10}$ nanowires exhibit a diameter from 100 to 300 nm and lengths up to micrometers, with bunch-like structure. With the assistance of S^{2-} etching and Kirkendall effect, structural evolution takes place from the original solid nanowire into a hollow structure. The SEM image reveals tubular hollow framework with thin shell (Fig. 1b). The Co_9S_8 tube is formed via structure induced anisotropic chemical etching by exchange reaction with S^{2-} ions initially on the surfaces of the solid nanowires sacrificial template. The unbalanced counter-diffusion of Co and S atoms then lead to Kirkendall void formation. With prolonged reaction, the core is continuously consumed whilst the void enlarged leading to nanotube structure. As shown by the TEM images shown in Fig. S1a-c, similar diameters and lengths were preserved except open ends, and the wall thickness is about

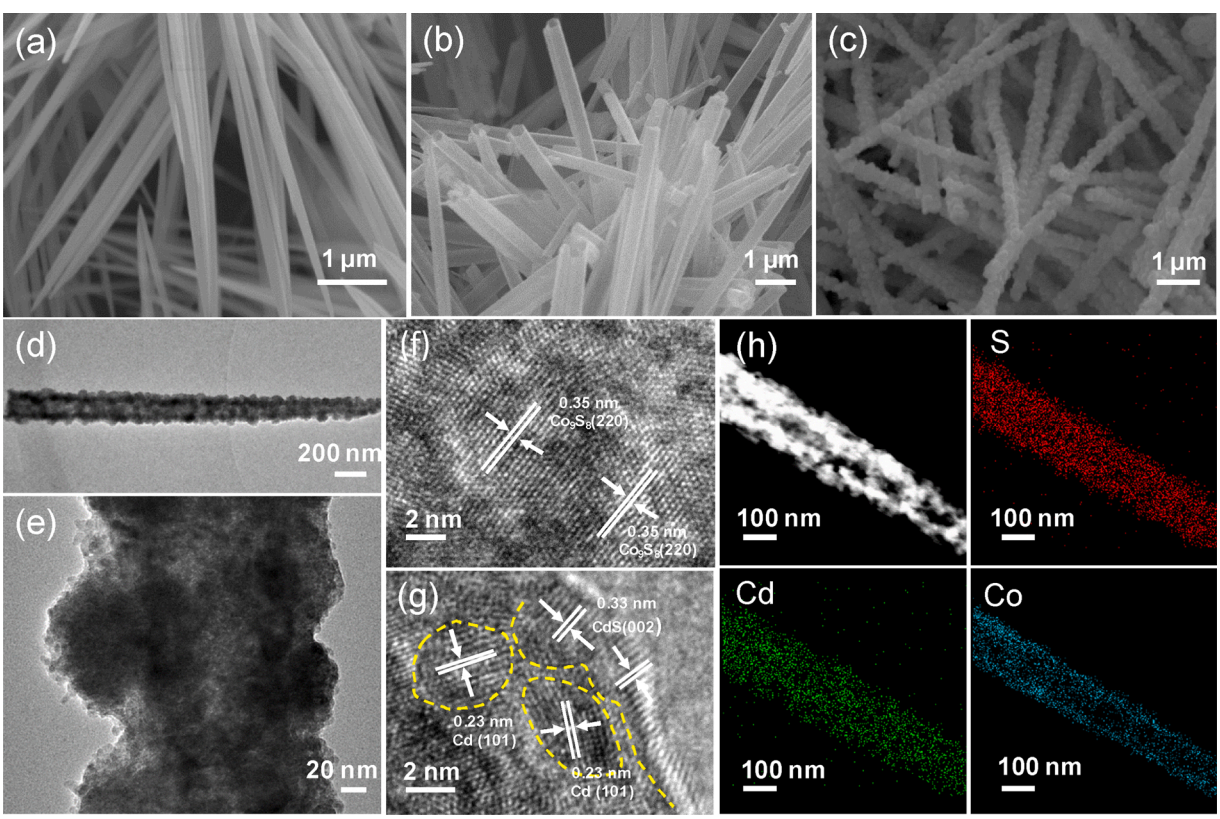

Fig. 1. SEM images of (a) $Co(CO_3)_{0.35}Cl_{0.20}(OH)_{1.10}$ nanowires, (b) Co_9S_8 nanotubes, and (c) Co_9S_8/Cd/CdS heterostructure. (d, e) Low and high magnified TEM images of Co_9S_8/Cd/CdS (CC-10). HRTEM images of (f) the nanotube part and (g) nanoparticle part of Co_9S_8/Cd/CdS (CC-10). (h) HAADF-TEM and EDX elemental mapping images of S, Cd, and Co.

10 nm. HAADF-STEM and EDX elemental mapping images (Fig. S1c) further confirm the successful tubular conversion, and uniform Co and S elements distribution covering the whole tube. Notably, this tubular conversion can enrich active sites density (Fig. S2 a–c), induce favorable mass flux and shorten electronic transport. In addition, the XRD patterns (Figs. S3 and S4) exhibit peaks matching to $Co(CO_3)_{0.35}Cl_{0.20}(OH)_{1.10}$ nanowires (JCPDS No.38−0547) are modified to the peaks referring to Co_9S_8 nanotubes (JCPDS Card No. 86-2273), further corroborate the chemical transformation.

The Cd/CdS nanoparticles were subsequently anchored onto the nanotubes to realize hierarchical Co_9S_8/Cd/CdS heterostructure *via* hydrothermal growth. As displayed in Fig. 1c, the optimized Co_9S_8/Cd/CdS sample denoted as CC-10 has a 1D hierarchical tubular heterostructure, in which Cd/CdS nanoparticles were uniformly and densely coated on the surface of individual Co_9S_8 nanotube. The representative TEM image of CC-10 in Fig. 1d further proves the coupling and even distribution of Cd/CdS nanoparticles along the Co_9S_8 nanotubes. The diameter of each Cd/CdS nanoparticle is about 100 ~ 150 nm (Fig. 1e). In sharp contrast, other Co_9S_8/Cd/CdS composites either present overloaded, aggregated and unattached Cd/CdS nanoparticles (Fig. S5 for CC-2 and Fig. S6 for CC-5), or sparse nanoparticles or bare Co_9S_8 nanotubes (Fig. S7 for CC-15). The optimal coverage of uniform Cd/CdS nanoparticles of CC-10 (Fig. S8) has a desirable nanotube-nanoparticle core-shell architecture that endows close integration and stable contact between the two photochemically active oxidation and reduction catalysts. High resolution TEM images of CC-10 (Figs. 1f, g and S9) show clear lattice fringes, and the lattice spacing of 0.35 nm corresponds to (220) plane of Co_9S_8, while 0.23 nm and 0.33 nm interplanar distances correspond to (101) crystal facet of Cd and (002) plane of CdS, respectively. Furthermore, HAADF-TEM and EDX elemental mapping images of a single CC-10 nanotube present a homogeneous distribution of S, Cd and Co elements (Fig. 1h).

3.2. Phase and composition analysis of the Co_9S_8/Cd/CdS tubular heterostructure

The crystal structure and phase composition of Co_9S_8, Cd/CdS, and CC-10 are evidenced by the X-ray diffraction (XRD) analysis. As shown in Fig. 2, multiple diffraction peaks located at 29.8°, 31.2°, 47.6°, 52.1° can be assigned to (311), (222), (511) and (440) planes of Co_9S_8 (JCPDS 86–2273), respectively. Characteristic peaks of Cd/CdS are 26.4°, 43.8°, 52.5° and 71.2° correspond to (111), (220), (311), and (331) planes of face-centered cubic CdS (JCPDS 75–1546), respectively. The obvious sharp diffraction peak at 38.4° is indexed to the (101) plane of Cd, which matches well with the HRTEM analysis, further indicating the co-existence of metallic Cd and semiconductor CdS in the heterogeneous Cd/CdS nanoparticles. As expected, all characteristic diffraction peaks of Co_9S_8, CdS and Cd can be observed in the CC-10 sample, validating the preservation of desired catalytic active components, demonstrating the strategy towards *in-situ* generation of conductive Cd metal electron bridge forming seamless hetero-metal chalcogenides tandem structure.

The elemental composition and surface chemical states of Co_9S_8, Cd/CdS, and CC-10 are analyzed by X-ray photoelectron spectroscopy (XPS) measurements. All Co, S and Cd elements can be clearly observed in the survey spectra of CC-10 (Fig. 3a). Fig. 3b–d further illustrate the high-resolution XPS spectra of Cd 3d, S 2p and Co 2p of CC-10. As displayed in Figs. 3b and S10, two peaks of Cd $3d_{5/2}$ (405.4 eV) and Cd $3d_{3/2}$ (414.9 eV) are assigned to Cd^{2+} for metal Cd, and the other peaks correspond to Cd^0 for CdS, which are consistent with the above XRD analysis [38,42]. The binding energy at 161.2 and 162.3 eV correspond to S $2p_{3/2}$ and S $2p_{1/2}$ orbitals of S^{2-} ions (Fig. 3c), in good agreement with the previous report [43,44]. The high-resolution Co 2p XPS spectrum in Fig. 3d revealed two spin-orbit doublets and two satellite peaks. The first doublet with binding energy of 778.6 and 781.2 eV and the second doublet with peaks at 793.6 and 797 eV are ascribed to Co$2p_{3/2}$ and Co$2p_{1/2}$, respectively, confirming the co-existence of Co^{2+} and Co^{3+} in consistent with the Co valence state of Co_9S_8 [45,46]. A shift in the binding energy of Co, S and Cd of CC-10 compared to bare Cd/CdS and Co_9S_8 was observed (Fig. S11 a–c), indicating a strong interaction between Co_9S_8 and Cd/CdS in the tubular heterostructure, thus, naturally establish the mediator bridge for efficient charge transfer.

3.3. Photocatalytic performance of the Co_9S_8/Cd/CdS tubular heterostructure

In view of the unique design and configuration of morphology and heterostructure in Co_9S_8/Cd/CdS, photocatalytic hydrogen evolution performance was then evaluated under visible light irradiation. For comparison purposes, Co_9S_8/Cd/CdS samples with different composition ratios, bare Cd/CdS, Co_9S_8, and CdS are tested as well. As shown in Fig. 4a, bare Co_9S_8 presents negligible H_2 yields even after 3 h of irradiation, which should be ascribed to the narrow band gap and fast recombination of photoinduced electrons and holes. Pristine Cd/CdS displays a H_2 production rate of 1.84 μmol h^{-1}, about 2.2 times more than pure CdS nanoparticles without metallic Cd (Fig. S12, 13), confirming the significant role of Cd as cocatalysts for charge transfer and electron-hole separation. Notably, control samples of Cd/CdS nanoparticles with the similar particle sizes as that in the Co_9S_8/Cd/CdS composite samples (Fig. S14) still exhibited a relatively low photoactivity (Fig. S15). However, greatly improved photocatalytic activity can be observed for all Co_9S_8/Cd/CdS composites, which exhibits steadily increasing H_2 generation over time. It can be seen that H_2 evolution is gradually enhanced with increased ratio of Co_9S_8 from 5.8 μmol h^{-1} for CC-2, 8.4 μmol h^{-1} for CC-5, and reached a maximum rate of 10.4 μmol h^{-1} on CC-10, which was approximately 5.7 times higher than that of bare Cd/CdS. An obvious decrease in H_2 yield (4.2 μmol h^{-1}) happens on CC-15 (Fig. 4b). That is to say, CC-10 shows an optimal light absorption and charge separation characteristics. More specifically, insufficient loading of Cd/CdS (CC-15) on Co_9S_8 could affect the light absorption and shorten active photoelectron lifetime for proton reduction, while overloading (CC-2 and CC-5) would lead to individual Cd/CdS nanoparticles with insufficient charge transfer and separation and H_2 evolution active sites. Importantly, the CC-10 showed an apparent quantum efficiency of 8.4 % at 380 nm and also exhibits excellent recyclability and photo-stability, and the H_2 generation rate of 10.4 μmol h^{-1} can keep steady at about without obvious drop even after five times cycles (Figs. 4c and S16).

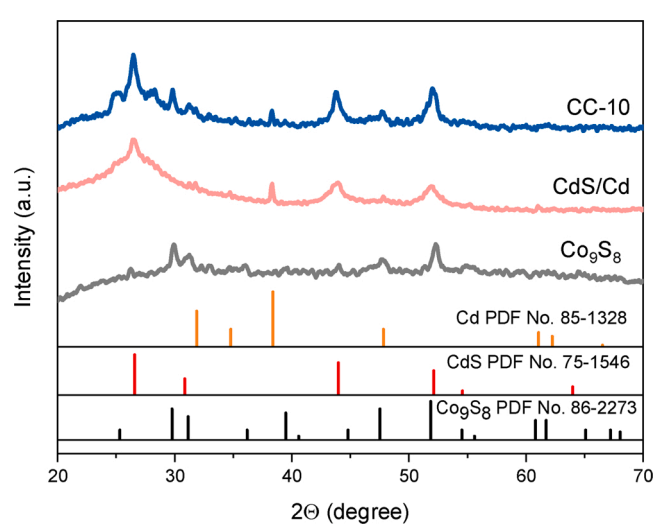

Fig. 2. X-ray diffraction patterns of Co_9S_8, Cd/CdS, and CC-10.

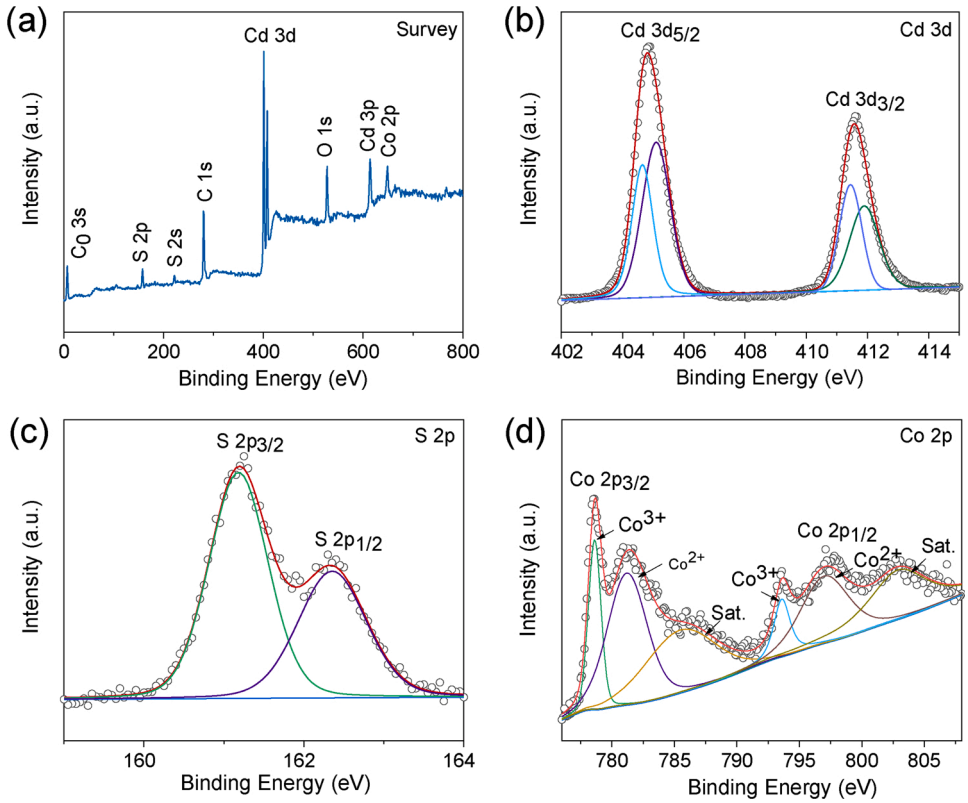

Fig. 3. (a) Survey X-ray photoelectron spectra of CC-10. High resolution XPS spectra of (b) Cd 3d, (c) S 2p, and (d) Co 2p.

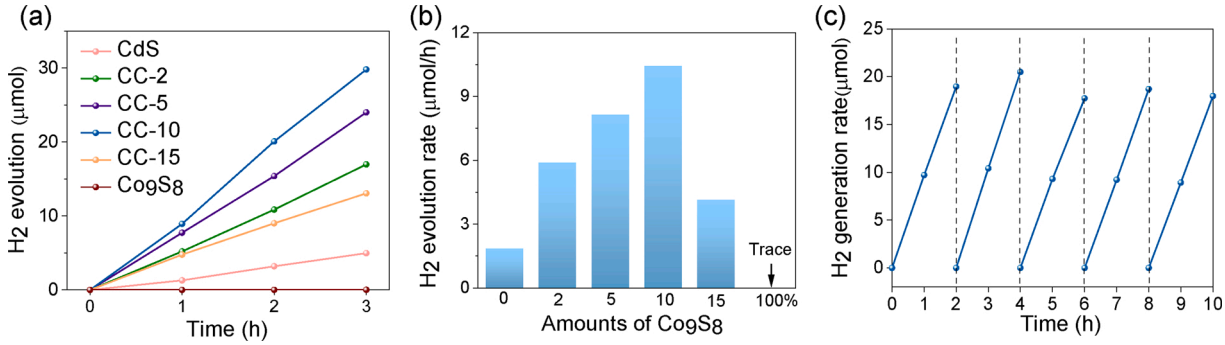

Fig. 4. (a) Amounts of H_2 generated from the prepared Co_9S_8, Cd/CdS, and Co_9S_8 /Cd/CdS composites over time under visible-light irradiation, (b) Photocatalytic H_2 evolution rates over the prepared samples, (c) Cycling test of photocatalytic H_2 evolution over CC-10. (Test conditions: light intensity of 100 mW/cm^2, 2 mg photocatalyst, 10 ml aqueous solution containing 0.35 M Na_2S and 0.25 M Na_2SO_3 as sacrificial reagents).

3.4. Photocatalytic mechanism of the Co_9S_8/Cd/CdS tubular heterostructure

In order to investigate the factors that contribute to the correlations between visible light absorption and photocatalytic activity. UV/Vis absorption spectroscopy is employed to evaluate the optical absorption range and intensity of Cd/CdS, Co_9S_8, and Co_9S_8/Cd/CdS compositions. As shown in Fig. 5a, b, Cd/CdS displayed an absorption edge at the position of about 541 nm related to a band gap of about 2.28 eV, while Co_9S_8 exhibited a very broad absorption in the whole range of 300–800 nm due to its narrow band gap of 1.23 eV. All Co_9S_8/Cd/CdS hybrids exhibited similar absorption edges with continually amplified absorption intensity with the increasing Co_9S_8 content. Correspondingly, a color transformation from bright yellow (Cd/CdS contribution) to dark grey (Co_9S_8 domination) was also observed (Fig. S17). This phenomenon indicates augmented visible light harvesting capability with the introduction of Co_9S_8. Additionally, Mott – Schottky (M–S) plots were also performed to determine the type and flat-band position of Co_9S_8 and CdS. As shown in Fig. 5c, when the linear part of M–S plots extended downward to the potential axis, we can read the flat position of Co_9S_8 and CdS as -0.95 eV and -0.66 eV, respectively. As the flat position of n-type semiconductor is almost equal to the conduction band (CB) potential, CB of Co_9S_8 and CdS are roughly -0.95 eV and -0.66 eV, respectively. Combined with their bandgap of Co_9S_8 and CdS, the band structure of valence band (VB) are calculated via the equation $E_{VB} = E_{CB} + E_g$. Detailed band structure and calculation results of composite were described in Fig. 5d.

Photo/electrochemical characterizations are then carried out to estimate the charge separation and transfer efficiency to gain insights into the photocatalytic mechanism. Photocurrent responses were firstly employed to probe the charge transport kinetics. Evidently, all samples presented high sensitivity to on-off light cycle (Fig. 6a). It can be observed that when the visible light was on, the photocurrent would increase and then drop immediately once the light was off. It was

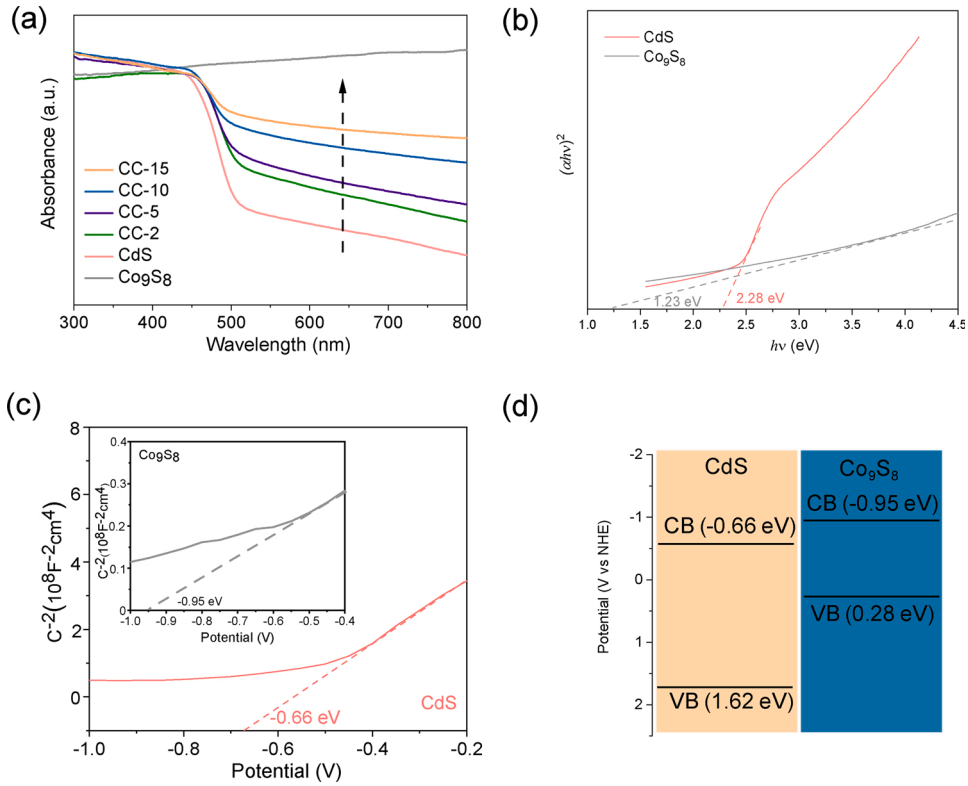

Fig. 5. (a) UV/Vis absorption spectra of all samples, (b) Plots of $(\alpha h\nu)^2$ versus $h\nu$ for CdS and Co_9S_8 samples, (c) Mott – Schottky plots of CdS and Co_9S_8 (inset image), (d) Schematic potential energy diagram of CdS and Co_9S_8.

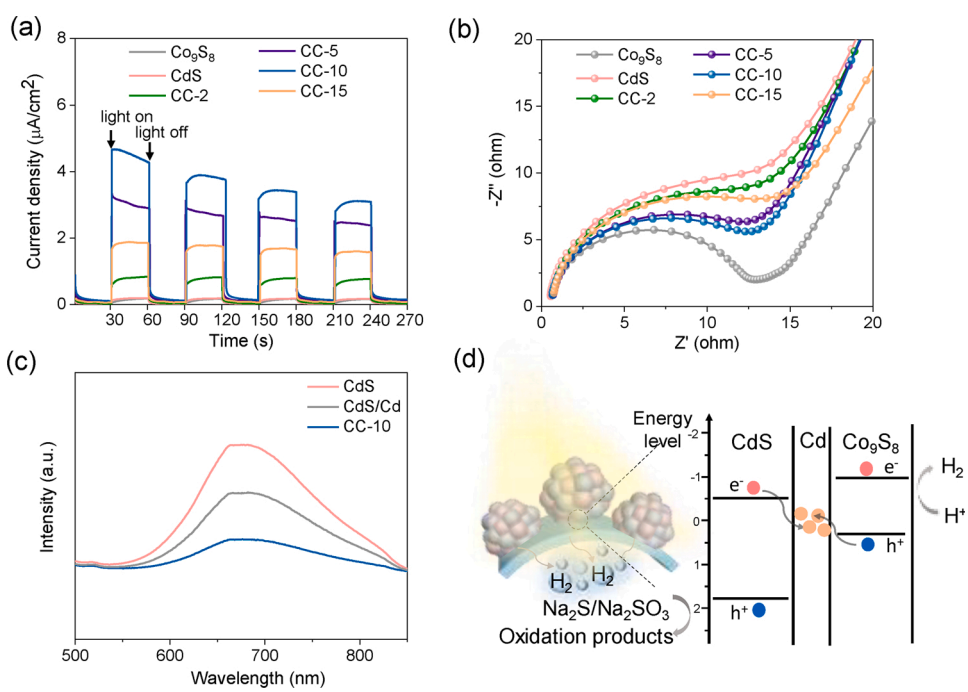

Fig. 6. (a) Photocurrent responses, and (b) Nyquist plots of as-prepared samples under visible-light irradiation, (c) Photoluminescence spectra of as-prepared CdS, Cd/CdS and CC-10, (d) Mechanism of charge transfer of Co_9S_8/Cd/CdS heterostructure.

noticeable that all Co_9S_8/Cd/CdS composites can generate much higher photocurrent density compared to the sole counterparts, and CC-10 exhibited the highest photocurrent. The higher photocurrent density of CC-10 signifies improved separation and transfer of photogenerated charge carriers as compared to the pristine CdS [47,48]. Noticeably, the photocurrent intensities of the various samples show consistent trend with that of H_2 production rates, demonstrating the crucial function of charge separation and migration efficiency towards boosting the photocatalytic activity. Simultaneously, Nyquist plots illustrates that the Co_9S_8/Cd/CdS composites had smaller arc radius than Cd/CdS (Fig. 6b),

indicating lower interfacial charge migration resistance, which can be attributed to better conductivity of Co_9S_8 (the smallest semicircle). Photoluminescence (PL) spectra was also taken to study charge carriers' kinetics. Fig. 6c shows the room temperature PL emission spectra of CdS, Cd/CdS and CC-10 that exhibit a broad peak due to band gap emission. Similar to the above photo/electrochemical analysis, the recombination of photo-induced electrons and holes is effectively suppressed in Co_9S_8/Cd/CdS, demonstrated by the much lower PL intensity of CC-10 than that of Cd/CdS and CdS. Consequently, the construction of Co_9S_8/Cd/CdS tubular heterostructure is proven to accelerate the separation and transfer of photogenerated charges efficiently, which favors excellent photocatalytic H_2 evolution.

In brief, a Z-scheme heterojunction with electron bridge among Co_9S_8/Cd/CdS was proposed and clarified in Fig. 6d. Due to the staggered band configuration between CdS and Co_9S_8, the in-situ reduced Cd metal would serve as an electron reservoir and transporter coupled with CdS and Co_9S_8 to form the all-solid-state Z-scheme system. Electrons on the CB of CdS and holes on the VB of Co_9S_8 would transfer through the in-situ reduced Cd metal, leading to the carrier recombination [49,50]. Consequently, photo-induced electrons on the CB of Co_9S_8 would be left to reduce protons to H_2, and holes on the VB of CdS would be consumed by sacrificial agent (Na_2S/Na_2SO_3). In this process, the metallic bridge of Z-scheme would prolong the lifetime of photo-generated charge carriers, thus promoting the photocatalytic H_2 evolution performance. To validate the Z-scheme mechanism, Pt deposition experiments were also performed to confirm the Z-scheme charge transfer pathway (Fig. S18). As shown in Fig. S19a, b, the Pt particles dispersed along Co_9S_8 rather than around CdS nanoparticles, implying that the electron charges remained at CB of Co_9S_8 were taken up for the reduction of metal salts instead of being transferred to CB of CdS. Taking into account the relative positions of CB potentials of CdS and Co_9S_8, and the intercalated metallic Cd, the construction of Z-scheme charge transfer process rather than type-II system could be confirmed.

4. Conclusion

In summary, a hollow Co_9S_8/Cd/CdS Z-scheme tubular heterostructure was rationally constructed via a facile hydrothermal method for enhanced photocatalytic hydrogen evolution. The synergistic coordination of hollow Co_9S_8 nanotube and Cd/CdS nanoparticles brings about high surface reactivity, broaden visible light absorption, and inhibition of photo-generated electron-hole pairs recombination, thus facilitating excellent photocatalytic performance. Furthermore, the locally formed Cd serves as internal metallic electronic channel between the reductive and oxidative photocatalysts to accelerate charge transport at the interface. As a result, the hierarchical Co_9S_8/Cd/CdS heterostructure with the optimized composition could achieve significantly enhanced photocatalytic H_2 generation rate, which was approximately 5.7 times higher than that of pristine Cd/CdS. This work will provide insight into the design and construction of promising Z-scheme photocatalysts for energy conversion applications.

CRediT authorship contribution statement

Tianxi Zhang: Conceptualization, Methodology, Formal analysis, Writing - original draft. **Fanlu Meng:** Project administration, Formal analysis, Validation, Writing - review & editing. **Yin Cheng:** Resources, Investigation. **Nikita Dewangan:** Resources, Investigation. **Ghim Wei Ho:** Formal analysis, Writing - review & editing, Supervision. **Sibudjing Kawi:** Supervision.

Declaration of Competing Interest

The authors declare that they have no known competing financial interests or personal relationships that could have appeared to influence the work reported in this paper.

Acknowledgements

The authors would gratefully thank the financial support from National University of Singapore, National Research Foundation, Prime Minister's Office, Singapore, the National Environment Agency under the Waste-to-Energy Competitive Research Program (WTE CRP 1501 103, WBS No. R-279-000-491-279), Agency for Science, Technology and Research (AME-IRG A1783c0016, WBS No. R-279-000-509-305) and Ministry of Education (MOE2017-T2-2-130, WBS No. R-279-000-544-112 and MOE2017-T2-1-140, WBS No. R-263-000-C85-112).

Appendix A. Supplementary data

Supplementary material related to this article can be found, in the online version, at doi:https://doi.org/10.1016/j.apcatb.2020.119853.

References

[1] S. Chen, T. Takata, K. Domen, Particulate photocatalysts for overall water splitting, Nat. Rev. Mater. 2 (2017) 1–17.
[2] J. Gong, C. Li, M.R. Wasielewski, Advances in solar energy conversion, Chem. Soc. Rev. 48 (2019) 1862–1864.
[3] C.S. Ponseca Jr., P. Chabera, J. Uhlig, P. Persson, V. Sundstrom, Ultrafast electron dynamics in solar energy conversion, Chem. Rev. 117 (2017) 10940–11024.
[4] S.D. Tilley, Recent advances and emerging trends in photo-electrochemical solar energy conversion, Adv. Energy Mater. 9 (2019) 1802877.
[5] E. Romero, V.I. Novoderezhkin, R. van Grondelle, Quantum design of photosynthesis for bio-inspired solar energy conversion, Nature 543 (2017) 355–365.
[6] T. Takata, K. Domen, Particulate photocatalysts for water splitting: recent advances and future prospects, ACS Energy Lett. 4 (2019) 542–549.
[7] Q. Wang, K. Domen, Particulate Photocatalysts for light-driven water splitting: mechanisms, challenges, and design strategies, Chem. Rev. 120 (2020) 919–985.
[8] T. Hisatomi, K. Domen, Reaction systems for solar hydrogen production via water splitting with particulate semiconductor photocatalysts, Nat. Catal. 2 (2019) 387–399.
[9] M.Q. Yang, M. Gao, M. Hong, G.W. Ho, Visible-to-NIR photon harvesting: progressive engineering of catalysts for solar-powered environmental purification and fuel production, Adv. Mater. 30 (2018) e1802894.
[10] Y. Bai, Y. Zhou, J. Zhang, X. Chen, Y. Zhang, J. Liu, J. Wang, F. Wang, C. Chen, C. Li, Homophase junction for promoting spatial charge separation in photocatalytic water splitting, ACS Catal. 9 (2019) 3242–3252.
[11] S.J.A. Moniz, S.A. Shevlin, D.J. Martin, Z.-X. Guo, J. Tang, Visible-light driven heterojunction photocatalysts for water splitting – a critical review, Energy Environ. Sci. 8 (2015) 731–759.
[12] A. Kudo, Y. Miseki, Heterogeneous photocatalyst materials for water splitting, Chem. Soc. Rev. 38 (2009) 253–278.
[13] K. Mitchell, J.A. Ibers, Rare-earth transition-metal chalcogenides, Chem. Rev. 102 (2002) 1929–1952.
[14] M.R. Gao, Y.F. Xu, J. Jiang, S.H. Yu, Nanostructured metal chalcogenides: synthesis, modification, and applications in energy conversion and storage devices, Chem. Soc. Rev. 42 (2013) 2986–3017.
[15] Y. Zhang, Q. Zhou, J. Zhu, Q. Yan, S.X. Dou, W. Sun, Nanostructured metal chalcogenides for energy storage and electrocatalysis, Adv. Funct. Mater. 27 (2017) 1702317.
[16] W.Y. Lim, H. Wu, Y.-F. Lim, G.W. Ho, Facilitating the charge transfer of $ZnMoS_4$/CuS p–n heterojunctions through ZnO intercalation for efficient photocatalytic hydrogen generation, J. Mater. Chem. A 6 (2018) 11416–11423.
[17] M. Shao, Y. Shao, S. Ding, R. Tong, X. Zhong, L. Yao, W.F. Ip, B. Xu, X.-Q. Shi, Y.-Y. Sun, Carbonized MoS_2: super-active co-catalyst for highly efficient water splitting on CdS, ACS Sustain. Chem. Eng. 7 (2019) 4220–4229.
[18] X. Li, J. Zhu, H. Li, Comparative study on the mechanism in photocatalytic degradation of different-type organic dyes on SnS_2 and CdS, Appl. Catal. B 123-124 (2012) 174–181.
[19] B. Han, S. Liu, N. Zhang, Y.-J. Xu, Z.-R. Tang, One-dimensional CdS@MoS_2 core-shell nanowires for boosted photocatalytic hydrogen evolution under visible light, Appl. Catal. B 202 (2017) 298–304.
[20] G. Zhang, D. Chen, N. Li, Q. Xu, H. Li, J. He, J. Lu, Preparation of $ZnIn_2S_4$ nanosheet-coated CdS nanorod heterostructures for efficient photocatalytic reduction of Cr (VI), Appl. Catal. B 232 (2018) 164–174.
[21] M. Ge, Q. Li, C. Cao, J. Huang, S. Li, S. Zhang, Z. Chen, K. Zhang, S.S. Al-Deyab, Y. Lai, One-dimensional TiO_2 nanotube photocatalysts for solar water splitting, Adv. Sci. 4 (2017) 1600152.
[22] C. Bie, B. Zhu, F. Xu, L. Zhang, J. Yu, In situ grown monolayer N-doped graphene on CdS hollow spheres with seamless contact for photocatalytic CO_2 reduction, Adv. Mater. 31 (2019) e1902868.
[23] Y. Huo, X. Yang, J. Zhu, H. Li, Highly active and stable CdS–TiO_2 visible photocatalyst prepared by in situ sulfurization under supercritical conditions, Appl. Catal. B 106 (2011) 69–75.
[24] W. Zhen, X. Ning, B. Yang, Y. Wu, Z. Li, G. Lu, The enhancement of CdS photocatalytic activity for water splitting via anti-photocorrosion by coating Ni_2P

shell and removing nascent formed oxygen with artificial gill, Appl. Catal. B 221 (2018) 243–257.
[25] Z. Jiang, K. Qian, C. Zhu, H. Sun, W. Wan, J. Xie, H. Li, P.K. Wong, S. Yuan, Carbon nitride coupled with CdS-TiO_2 nanodots as 2D/0D ternary composite with enhanced photocatalytic H_2 evolution: a novel efficient three-level electron transfer process, Appl. Catal. B 210 (2017) 194–204.
[26] J. Low, C. Jiang, B. Cheng, S. Wageh, A.A. Al-Ghamdi, J. Yu, A review of direct Z-scheme photocatalysts, Small Methods 1 (2017) 1700080.
[27] L.J. Zhang, S. Li, B.K. Liu, D.J. Wang, T.F. Xie, Highly efficient CdS/WO_3 photocatalysts: Z-scheme photocatalytic mechanism for their enhanced photocatalytic H_2 evolution under visible light, ACS Catal. 4 (2014) 3724–3729.
[28] J. Jin, J. Yu, D. Guo, C. Cui, W. Ho, A hierarchical Z-scheme CdS–WO_3 photocatalyst with enhanced CO2 reduction activity, Small 11 (2015) 5262–5271.
[29] S. Sun, J. Luo, Y. Qian, Y. Jin, Y. Liu, Y. Qiu, X. Li, C. Fang, J. Han, Y. Huang, Metal–organic framework derived honeycomb Co_9S_8@ C composites for high-performance supercapacitors, Adv. Energy Mater. 8 (2018) 1801080.
[30] L. Wang, S. Li, F. Huang, X. Yu, M. Liu, H. Zhang, Interface modification of hierarchical Co_9S_8@ NiCo layered dihydroxide nanotube arrays using polypyrrole as charge transfer layer in flexible all-solid asymmetric supercapacitors, J. Power Sources 439 (2019) 227103.
[31] S. Wang, B.Y. Guan, X. Wang, X.W.D. Lou, Formation of Hierarchical Co_9S_8@ $ZnIn_2S_4$ heterostructured cages as an efficient photocatalyst for hydrogen evolution, J. Am. Chem. Soc. 140 (2018) 15145–15148.
[32] H. Zhu, B. Yang, J. Xu, Z. Fu, M. Wen, T. Guo, S. Fu, J. Zuo, S. Zhang, Construction of Z-scheme type CdS–Au–TiO_2 hollow nanorod arrays with enhanced photocatalytic activity, Appl. Catal. B 90 (2009) 463–469.
[33] J. Xu, W.-M. Yang, S.-J. Huang, H. Yin, H. Zhang, P. Radjenovic, Z.-L. Yang, Z.-Q. Tian, J.-F. Li, CdS core-Au plasmonic satellites nanostructure enhanced photocatalytic hydrogen evolution reaction, Nano Energy 49 (2018) 363–371.
[34] X. Wu, J. Zhao, L. Wang, M. Han, M. Zhang, H. Wang, H. Huang, Y. Liu, Z. Kang, Carbon dots as solid-state electron mediator for $BiVO_4$/CDs/CdS Z-scheme photocatalyst working under visible light, Appl. Catal. B 206 (2017) 501–509.
[35] X.-B. Meng, J.-L. Sheng, H.-L. Tang, X.-J. Sun, H. Dong, F.-M. Zhang, Metal-organic framework as nanoreactors to co-incorporate carbon nanodots and CdS quantum dots into the pores for improved H_2 evolution without noble-metal cocatalyst, Appl. Catal. B 244 (2019) 340–346.
[36] H. Zhang, L. Zhao, F. Geng, L.-H. Guo, B. Wan, Y. Yang, Carbon dots decorated graphitic carbon nitride as an efficient metal-free photocatalyst for phenol degradation, Appl. Catal. B 180 (2016) 656–662.
[37] W. Zhong, S. Shen, M. He, D. Wang, Z. Wang, Z. Lin, W. Tu, J. Yu, The pulsed laser-induced Schottky junction via in-situ forming Cd clusters on CdS surfaces toward efficient visible light-driven photocatalytic hydrogen evolution, Appl. Catal. B 258 (2019) 117967.
[38] Q. Wang, J. Li, Y. Bai, J. Lian, H. Huang, Z. Li, Z. Lei, W. Shangguan, Photochemical preparation of Cd/CdS photocatalysts and their efficient photocatalytic hydrogen production under visible light irradiation, Green Chem. 16 (2014) 2728–2735.
[39] N. Bao, L. Shen, T. Takata, K. Domen, A. Gupta, K. Yanagisawa, C.A. Grimes, Facile Cd− thiourea complex thermolysis synthesis of phase-controlled CdS nanocrystals for photocatalytic hydrogen production under visible light, J. Phys. Chem. C 111 (2007) 17527–17534.
[40] L. Shang, B. Tong, H. Yu, G.I. Waterhouse, C. Zhou, Y. Zhao, M. Tahir, L.Z. Wu, C. H. Tung, T. Zhang, CdS nanoparticle-decorated Cd nanosheets for efficient visible light-driven photocatalytic hydrogen evolution, Adv. Energy Mater. 6 (2016) 1501241.
[41] Y. Guo, J. Wang, Z. Tao, F. Dong, K. Wang, X. Ma, P. Yang, P. Hu, Y. Xu, L. Yang, Facile synthesis of mesoporous CdS nanospheres and their application in photocatalytic degradation and adsorption of organic dyes, Cryst. Eng. Comm. 14 (2012) 1185–1188.
[42] W. Li, M. Li, S. Xie, T. Zhai, M. Yu, C. Liang, X. Ouyang, X. Lu, H. Li, Y. Tong, Improving the photoelectrochemical and photocatalytic performance of CdO nanorods with CdS decoration, Cryst. Eng. Comm. 15 (2013) 4212–4216.
[43] S. Li, L. Wang, Y. Li, L. Zhang, A. Wang, N. Xiao, Y. Gao, N. Li, W. Song, L. Ge, J. Liu, Novel photocatalyst incorporating Ni-Co layered double hydroxides with P-doped CdS for enhancing photocatalytic activity towards hydrogen evolution, Appl. Catal. B 254 (2019) 145–155.
[44] R.-B. Wei, Z.-L. Huang, G.-H. Gu, Z. Wang, L. Zeng, Y. Chen, Z.-Q. Liu, Dual-cocatalysts decorated rimous CdS spheres advancing highly-efficient visible-light photocatalytic hydrogen production, Appl. Catal. B 231 (2018) 101–107.
[45] X. Li, K. Li, S. Zhu, K. Fan, L. Lyu, H. Yao, Y. Li, J. Hu, H. Huang, Y.W. Mai, J. B. Goodenough, Fiber-in-tube design of Co_9S_8-Carbon/Co_9S_8: enabling efficient sodium storage, Angew. Chem. Int. Ed. 58 (2019) 6239–6243.
[46] J. Liu, C. Wu, D. Xiao, P. Kopold, L. Gu, P.A. van Aken, J. Maier, Y. Yu, MOF-derived hollow Co_9S_8 nanoparticles embedded in graphitic carbon nanocages with superior Li-ion storage, Small 12 (2016) 2354–2364.
[47] S.W.L. Ng, M. Gao, W.L. Ong, K.J.H. Lim, C.K.N. Peh, G.W. Ho, Simultaneous in situ reduction and embedment of Cu nanoparticles into TiO_2 for the design of exceptionally active and stable photocatalysts, J. Mater. Chem. A 6 (2018) 16213–16219.
[48] S.W.L. Ng, G. Yilmaz, W.L. Ong, G.W. Ho, One-step activation towards spontaneous etching of hollow and hierarchical porous carbon nanospheres for enhanced pollutant adsorption and energy storage, Appl. Catal. B 220 (2018) 533–541.
[49] P. Tan, Y. Liu, A. Zhu, W. Zeng, H. Cui, J. Pan, Rational design of Z-scheme system based on 3D hierarchical CdS supported 0D Co_9S_8 nanoparticles for superior photocatalytic H_2 generation, ACS Sustain. Chem. Eng. 6 (2018) 10385–10394.
[50] B. Qiu, Q. Zhu, M. Du, L. Fan, M. Xing, J. Zhang, Efficient solar light harvesting CdS/ Co_9S_8 hollow cubes for Z-Scheme photocatalytic water splitting, Angew. Chem. Int. Ed. 56 (2017) 2684–2688.